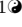
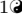



A model for the size distribution of marine microplastics: a statistical mechanics approach

Kunihiro Aoki¹, Ryo Furue¹,

¹ Japan Agency for Marine-Earth Science and Technology, Yokohama, Kanagawa, Japan

 These authors contributed equally to this work.

* kaoki@jamstec.go.jp

Abstract

The size distribution of marine microplastics provides a fundamental data source for understanding the dispersal, break down, and biotic impacts of the microplastics in the ocean. The observed size distribution at the sea surface generally shows, from large to small sizes, a gradual increase followed by a rapid decrease. This decrease has led to the hypothesis that the smallest fragments are selectively removed by sinking or biological uptake. Here we propose a new model of size distribution without any removal of material from the system. The model uses an analogy with black-body radiation and the resultant size distribution is analogous to Planck's law. In this model, the original large plastic piece is broken into smaller pieces once by the application of "energy" or work by waves or other processes, under two assumptions, one that fragmentation into smaller pieces requires larger energy and the other that the probability distribution of the "energy" follows the Boltzmann distribution. Our formula well reproduces observed size distributions over wide size ranges from micro- to mesoplastics. According to this model, the smallest fragments are fewer because large "energy" required to produce such small fragments occurs more rarely.

Introduction

A large fraction of the estimated billion tonnes of plastic waste that goes into the ocean [1] is found in a fragmented form, "microplastics", with sizes of less than 5 mm [2] through photodegradation and weathering processes [3–5]. Those microplastics spread globally [6–9], potentially acting as a transport vector of chemical pollutants [10–12] and causing physical and chemical damages on marine organism [13–15]. Recent drift simulations of microplastics calibrated against observed abundance of microplastics have produced global or semi-global maps of estimated microplastics abundance and concentration near the sea surface [6–8]. These simulations will be further used to assess the biological impacts of microplastics.

Such simulations generally assume the size distribution of microplastics and their results would depend on the assumption because sedimentation and biological uptake can depend on size [14, 16–18]. Interestingly, the number of small pieces rapidly decreases toward smaller sizes of $O(100\ \mu\text{m})$ in most observations of plastic fragments at the sea surface [19–22]. This feature is puzzling because the number of plastic pieces is expected to increase toward smaller sizes if the pieces keep broken down into smaller and smaller pieces (progressive fragmentation). For example, Cózar et al. [20] indicates that a type of progressive fragmentation leads to a cube law toward smaller sizes. The

observed decrease at smaller sizes has generally been hypothesized to be due to selective sinking to depths, sampling error, or to selective ingestion by marine organisms [19–21, 23–25].

The fracture mechanisms of marine plastics, however, are not well known. The power law, which results from scale-invariant fracture processes, is often invoked to explain observed size distributions of plastics. It tends to fit well observed size distributions at larger sizes [20]. The power law can be derived, for example, from collision cascade among objects, as often applied to the fragmentation of asteroids [26–28], which does not include any decrease toward smaller sizes unless or until other processes than fragmentation start to dominate. Somewhat different fragmentation processes lead to a log-normal distribution [29–31], which is premised on the size reduction rate following the Normal distribution and has been applied to the fragmentation of sand grains, mastication, and the fracturing of thin glass rods [32–34], but not to oceanic microplastics to our knowledge. The log-normal distribution has a peak skewed toward smaller sizes and is similar to observed size distributions of fragments at smaller sizes but tends to deviate from observed distribution at larger sizes, where the power law tends to fit better [20]. To the best of our knowledge, only the Weibull distribution [35, 36] is similar to observed size distributions across the microplastics and mesoplastics ranges (fragments larger than 5 mm), at least in Cózar et al.’s study [20]. The Weibull distribution as applied to the size distributions of various types of particles is largely empirical but with an interpretation as resulting from the branching tree of cracks [36].

In this paper, we propose a new model where “energy” needed to break down the plastic pieces acts as a constraint. We assume that the probability of the “energy” obeys the Boltzmann distribution. The statistics of fragmentation is then analogous to that of the black body radiation and the resultant size distribution is analogous to the Planck distribution. As we shall see, without the assumption of selective sinking or ingestion, this size distribution has a peak skewed toward small sizes and the smaller plastic pieces beyond the peak are much scarcer. We also discuss the generation of finer microplastics ($O(10\ \mu\text{m})$), which is recently observed mostly in the mixed layer, in terms of our fracture model.

Fracture model

We assume that plastic waste first becomes fragile on beaches because of ultraviolet light and other weathering factors and then is broken up on beaches into microplastic pieces by the action of waves, winds, and other forces before being washed off into the ocean. Accordingly, the amount (mass) of microplastics which is produced on beaches will be determined by these processes. The fraction of microplastics that goes into the ocean may depend on waves and other weather factors. The microplastics will then be diluted in the ocean by mixing due to turbulence. These are the microplastics which observations sample. In the following we build a simple, idealized statistical model that determines the size distribution of the microplastics produced on the beaches. The model considers the fragmentation of given plastic mass and is naturally mass-conserving.

We offer the following simple physical model only as a representation of complicated fragmentation processes such as one-time crush and slow weathering. We do not claim that the following are exactly the underlying processes that lead to the observed size distribution. This model is originally intended to explain microplastics larger than $O(100\ \mu\text{m})$. It will be later extended for finer microplastics (see the Discussion section and [S4 Appendix](#)). In this section, we only show an outline of the derivation. Details are found in “[Details of fracture model](#)” of the Materials and Methods section.

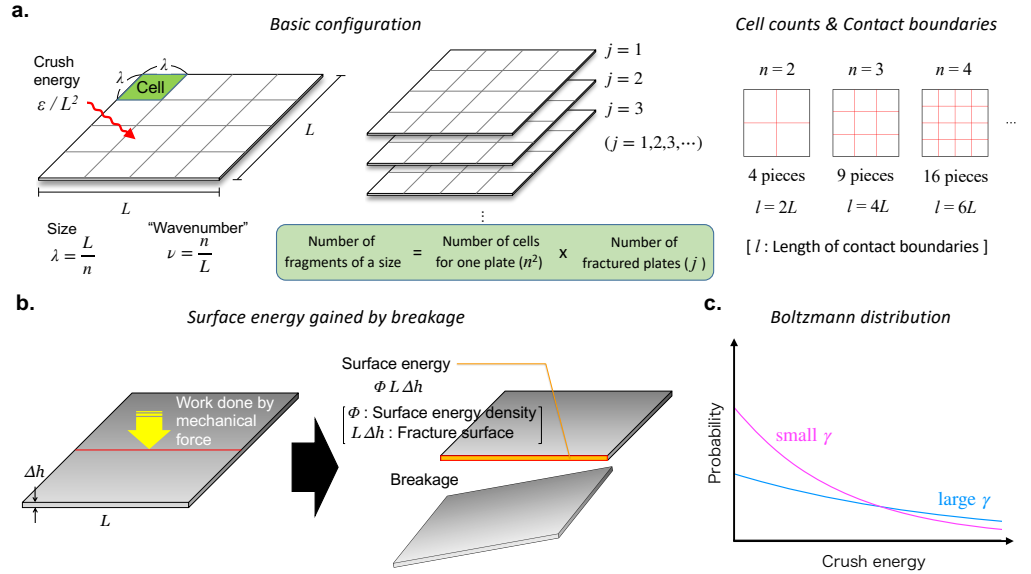


Fig 1. Schematic illustration of model configuration. **a.** Schematic representation of our fracture model. An idealized plastic plate with a size of $L \times L$ and a thickness of Δh is broken into $n \times n$ equal-sized pieces. The size of each broken piece is $\lambda = L/n$ (left). The total length of the contact boundaries (red lines) is obviously $l \equiv 2(n-1)L$ (right). We sum up energy needed to break j plates into λ -sized pieces and denote it as ε (middle). **b.** Schematic representation of breakage. Energy needed to break up the plate is proportional to the cross-sectional area of the contact boundary and hence to the length of the fracture. **c.** Occurrence probability of crush energy governed by the Boltzmann distribution, $p(\varepsilon) = e^{-\varepsilon/\gamma}/\gamma$, which exponentially decreases for larger crush energy ε . The e-folding scale is γ and hence the probability of larger crush energy becomes larger as γ increases.

The model assumes that the original plastic piece is a square plate with a size of $L \times L$ and a uniform thickness of Δh . This plate is broken into $n \times n$ equal-sized cells (Fig. 1a). In this case, the size of each broken piece is $\lambda = L/n$. The number of the fragments of this particular size is given by n^2 multiplied by the number of the original plates (Fig. 1a).

The fragmentation is assumed to be caused by some mechanical force and the required ‘‘crush energy’’ is assumed to be proportional to the total length of the fractures. This assumption may be justified by equating the crush energy to the surface energy of the newly created surfaces (Fig. 1b), the latter in general equal to the minimal work required in the failure of solid material [37,38]. Because the total area of the new surfaces is proportional to the total length of the contact boundaries for a plate (Fig. 1a, right) and because the surface energy is proportional to the area of the new surfaces [37,38], the crush energy is proportional to the total length of the fracture. To produce smaller pieces requires larger energy, which ultimately limits the number of small fragments as shall be seen below. This is the most significant new element of our model.

Plastic pieces are fragmented by the action of waves, winds, or sand under various conditions, for example, on a hard reef or on soft sand, and therefore energy exerted on the plastic pieces is considered random. Unless each of these processes is modeled in detail, however, it is impossible to calculate the probability distribution of the energy from first principles. Nor is it possible to infer the probability distribution from field measurements at present. To make progress, we assume that the Boltzmann

distribution, $p(\varepsilon) \propto e^{-\varepsilon/\gamma}$, governs the occurrence probability of crush energy ε (Fig. 1c). This distribution is often assumed *by default* when details of the underlying stochastic processes are not known and the distribution is known to be applicable to a wide variety of situations [39–42]. This generality comes from the fact that it is the distribution that maximizes the entropy under fixed total energy [43]; that is, it is the most probable energy distribution under fixed total energy. According to this probability distribution, a crush event with a large energy value is less frequent, consistent with common expectation. The factor γ may be regarded as a representative energy level of *the environment*, which represents the aggregate impacts of the combination of weather conditions (winds, waves, etc.) and the background conditions (hard or soft surfaces, etc.). We however note that the long-term statistics of the coastal wave height generally shows that a larger wave height occurs with a smaller frequency [44–46], qualitatively consistent with the Boltzmann distribution. Nevertheless, our main justification of using this distribution is that our theoretical prediction agrees well with observation as shown below.

The number of the fragments of a particular size is n^2j for a single crush event (Fig. 1a). Since crush events occur randomly, the size spectrum is the expected value of n^2j as a function of λ . Calculating the expected value with use of $n = L/\lambda$, we arrive at the size spectrum (see “**Details of fracture model**” of the Materials and Methods section)

$$S(\lambda)d\lambda = \frac{A}{\lambda^4} \frac{1}{e^{b/\lambda\gamma} - 1} d\lambda, \quad (1)$$

where A is an arbitrary positive constant, which is adjusted by the amount of the total mass of plastics to be fractured. Eq. 1 is analogous to the Planck’s energy spectrum of the black body radiation. See **S2 Appendix** for the analogy.

This size distribution has a shape skewed to smaller sizes similarly to the observed size distribution of the microplastics, as shown in Fig. 2. For a fixed A , the size distribution is controlled by γ and b . The factor b depends on the plastic material and the size of the original plate. The increase of γ and the decrease of b , however, have the same effect on controlling the size distribution and hence we introduce a new parameter $\gamma^* \equiv \gamma/b$. This parameter measures the strength of the mean environmental energy against the strength of the plastic material and its inverse provides a characteristic size such that the peak size, λ_p , is given by $\lambda_p \simeq 0.255\gamma^{*-1}$. As this parameter increases, thus, the size at which the maximum of the size distribution occurs decreases like γ^{*-1} and the corresponding maximum value increases like γ^{*4} (Fig. 2a). Furthermore, in the large size limit, i.e., $\lambda\gamma^* \gg 1$, this size distribution asymptotes to $S(\lambda)d\lambda \sim A\gamma^*/\lambda^3 d\lambda$ (Fig. 2b), consistent with the cube power law observed in the mesoplastic range [20].

The total abundance and mass of the fragments for $\lambda < \Lambda$ ($\leq L$) are obtained, respectively, as

$$\begin{aligned} N &\equiv \int_0^\Lambda S(\lambda)d\lambda \approx \int_0^\infty S(\lambda)d\lambda = \sigma A\gamma^{*3}, \\ M &\equiv \int_0^\Lambda \rho\Delta h\lambda^2 S(\lambda)d\lambda = \rho\Delta h A\gamma^* \ln(1 - e^{-1/\gamma^*\Lambda}) \approx \rho\Delta h A\gamma^* \ln(\gamma^*\Lambda), \end{aligned} \quad (2)$$

where $\sigma \equiv 2.404$ (**S1 Appendix**), ρ is the plastic density, and Λ is the maximum size of plastic fragments. Both of the above approximations are for $\gamma^*\Lambda \gg 1$, that is, Λ being sufficiently larger than the characteristic size λ_p . See **S1 Appendix** for details.

We fit our model (1) to an observed size spectrum by adjusting A and γ^* . Observed size distributions are presented in various ways: as the number per unit volume of sampled sea water, as the number per unit surface area of the ocean, as the raw number

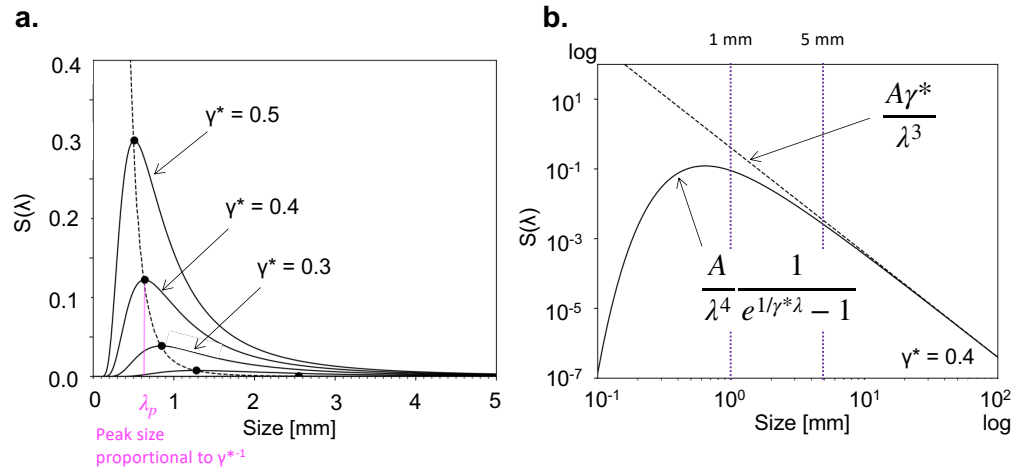


Fig 2. Theoretical size spectrum. **a.** size distributions expected from (1) for different values of γ^* under a fixed A ($= 1.0$). The dashed curve connects the peaks of the size distributions. **b.** a log-log plot of the same distribution for $\gamma^* = 0.4$ and $A = 1.0$ (solid curve). The dashed line denotes the power law $A\gamma^*/\lambda^3$, which the size-distribution curve asymptotes to for large λ .

of collected fragments, etc. Some studies normalize the spectrum so that $\int S(\lambda)d\lambda = 1$ [24, 25, 47]. However, note that the size spectrum (1) can take any of these forms by adjusting A and different representations of the same spectra do not affect our analysis because the differences are absorbed into A .

We begin by comparing the present theory with the observed size distribution obtained by Isobe et al [21]. This size distribution is based on the collection of plastic fragments sampled around Japan (Fig. 3a); this is the largest collection with the highest size resolution to date. For a precise comparison, we have converted the original size histogram into spectral density. Details are shown in “Observed data in Isobe et al” of the Materials and Methods section.

Application to observed data.

Theoretical curve is fitted to the observed size spectrum by adjusting the parameters A and γ^* by a least-squares method over $\lambda < 5$ mm. The theoretical curve fits the observed size distribution well over the whole microplastic range (Fig. 3b) with the relative error, $\text{Err} = 7\%$. (The relative error is defined by the norm of difference between the theoretical and observed size distributions divided by the norm of the observed size distribution.) For comparison, we also plot a lognormal distribution, $a\text{LN}(\mu, \sigma^2)$, with an amplification or normalization factor a , where the parameters a , μ , and σ are determined by the same least-squares method. The lognormal distribution is not much different from our model in this size range.

Our model also agrees well with the observed size distributions in the Western-Pacific transoceanic section ($\text{Err} = 22\%$) and the Seto Inland Sea ($\text{Err} = 21\%$) (Figs. 3c and d) with somewhat larger error than around Japan. The observed spectra are not as smooth as that around Japan, suggesting that the samples are not sufficient to give smooth distribution and this may be the reason for the larger error. Also, the peak is located at a smaller size in the Seto Inland Sea than in the other two regions; this shift is reflected in a larger value of γ^* . The lognormal distribution is somewhat more different from our model in these two regions (Figs. 3c and d) than in the area surrounding Japan (Fig. 3b). The empirical fitting curve used in Isobe et al [8] has

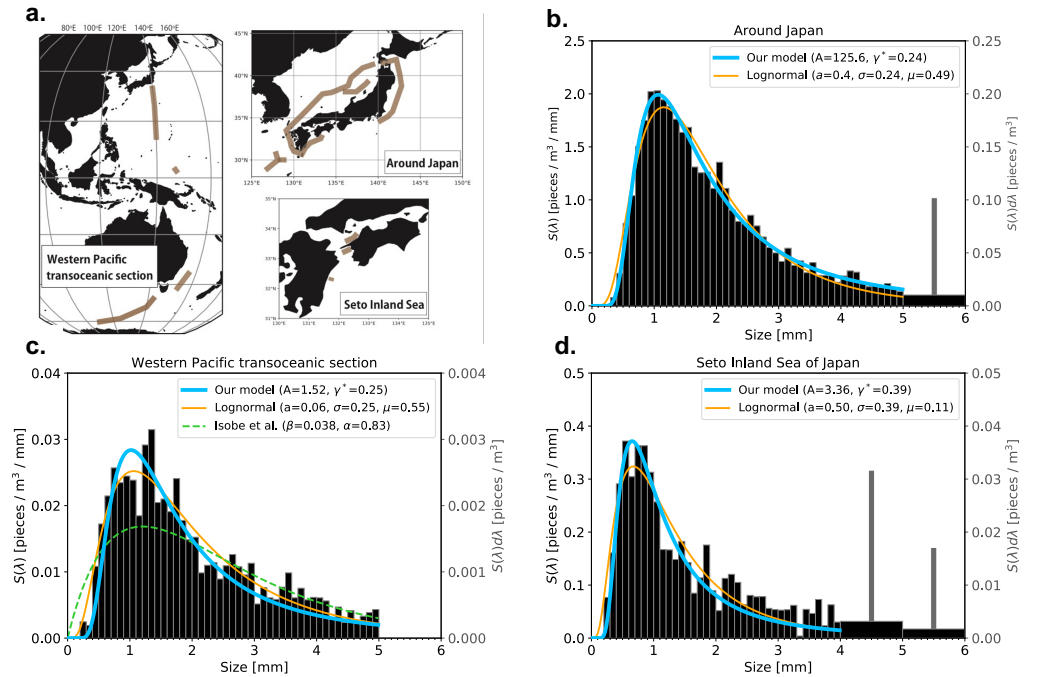


Fig 3. Comparison of theoretical size spectrum with the observed size distributions of Isobe et al [8, 19, 21]. **a.** Schematic map of observation stations in Isobe et al [8, 19, 21]. See their original papers for the detailed locations. **b–d.** Theoretical and observed size spectral densities of microplastics in the area surrounding Japan, along a Western-Pacific transoceanic section, and in the Seto Inland Sea. The black bars display the observed size spectral density (left axis), and gray bars are the original histogram (right axis) taken from Isobe et al. In the range $\lambda < 5$ mm, the black and gray rectangles perfectly coincide. See “Observed data in Isobe et al” in the Method section for the detailed method of the conversion from the histogram to the spectrum. The blue and orange curves denote our model and the lognormal distribution, respectively. The parameter A is dimensionless ($\times 10^{-9}$) in this case. The green dashed curve in **c** denotes the empirical curve $\beta\lambda e^{-\alpha\lambda}$ of Isobe et al [8]. The map in **a** is created using Cartopy (version 0.18) (<https://scitools.org.uk/cartopy>) embedded in Python and Adobe Illustrator CS6 (version 691) (<https://www.adobe.com>).

larger error, despite having the same number of parameters as ours (Fig. 3c).

We next compare our model with another set of observations summarized by C3zar et al [20] (Fig. 4a) based on samples collected in the accumulation zones (“garbage patches”) over the globe, where microplastics originating from coastal areas tend to converge by ocean currents [48, 49]. C3zar et al’s method of sampling plastic fragments is similar to Isobe et al’s [8, 19, 21], but their size distributions include more size bins in the mesoplastic range than Isobe et al’s (See “Observed data in C3zar et al” of the Materials and Methods section). Our model generally reproduces well the observed size distributions although it has large relative error in the South Pacific Ocean (Fig. 4b), where the least number of samples were collected in C3zar et al.’s study and the spectrum is the least smooth (barely visible in the plot), suggesting that the number of samples is not sufficient. The unweighted sum of the five size distributions is shown in Figure 4d in a log-log form. Importantly, the model reproduces the cube power law toward the mesoplastic range (Blue curve in Fig. 4d) as found by C3zar et al. The theoretical curve is not particularly good in the smallest size range, but this discrepancy reduces (gray curve and symbols in Fig. 4d) when we exclude the South Atlantic Ocean, which has large difference from the model in the sizes smaller than 0.5 mm (green curve and symbols in Fig. 4b). If the plastic pieces sampled in the South Atlantic came from different regions with a wide variety of γ^* values, this discrepancy may be explained (Figs. B and C in S3 Appendix). In contrast, the lognormal distribution does not follow the cube power law in the large size range (orange curve in Fig. 4d) and this discrepancy exists also in the case without the South Atlantic data (not shown). Despite having one more adjustable parameter, the log-normal distribution fit the data less well than our model.

The fitting of our model to observations gives a geographical distribution of γ^* . The γ^* value for C3zar et al’s observation is largest in the Pacific Oceans, smallest in the North Atlantic, and inbetween elsewhere (Fig. 4c). Given that the plastics are likely to be fragmented on beaches possibly by ocean waves [4], the value of γ^* would represent wave energy on beaches where plastic waste is littered or comes ashore before fragmented there and washed away into the ocean as micro- or mesoplastics. A scenario-based numerical experiment (see “Wave energy in source region” of the Materials and Methods section) suggests that the coastal area located along the western boundary of each basin is likely the major source region for the plastics in each accumulation zone, except that a large fraction of the plastics in the South Indian Ocean comes from South East Asia [48]. Compared with a map of categorized wave energy levels along the world coastlines [50], the wave energy level in the potential source regions for a basin (Table 1) appears correlated with the γ^* value for the accumulation zone of the basin in the emission scenario considering impervious area of land (Fig. 4c; the results for the other scenario are found in Table 1 and S1 Figure). The only exception is the North Pacific: the North Pacific accumulation zone has a large γ^* value in spite of the relatively small wave energy level in the South China Sea, likely the major source region for the North Pacific. In fact, a large fraction of the plastic emission from the East China Sea is likely to come ashore on the southern coast of Japan [48], where the wave energy level is large (Table 1). If the majority of plastic waste is fragmented there, therefore, the large γ^* value for the North Pacific may be explained (Fig. 4c).

The interpretation of γ^* for Isobe et al’s observations is less straightforward because the source region is less clear. The relatively low value of γ^* for the area surrounding Japan (Fig. 3b and S1 Table) may be due to the low wave energy in the East China Sea, which may be the source region of the microplastics [48]. In contrast, there are clearly multiple source regions contributing to the Western Pacific transoceanic section and it is possible that the distribution is a superposition of distributions with different γ^* values (Fig. B in S3 Appendix). It is interesting that the Seto Inland Sea has a very large γ^*

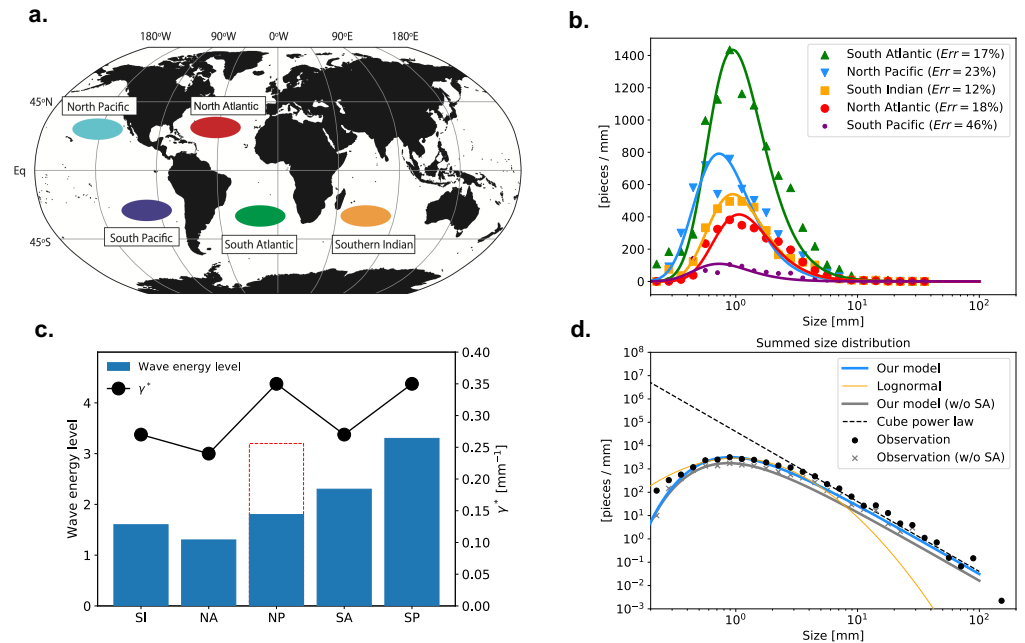


Fig 4. Application of theoretical model to Cózar et al [20]’s observational data and comparison between γ^* and wave energy. **a.** Schematic map of observation stations in Cózar et al [20]. See the original paper for the detailed locations. **b.** Theoretical (curves) and observed (symbols) size spectral density of all samples for each accumulation zone. The observed data are same as those in their Fig.S6, except that the values are expressed as a spectral density (see “Observed data in Cózar et al” in the Materials and Methods section). **c.** Expected wave energy levels (no units) at source regions (rectangles) and γ^* (dots) for accumulation zones. The accumulation zones are denoted by abbreviations such as SI for South Indian Ocean. The red dashed rectangle shows the wave energy level for the North Pacific Ocean in the case where the contribution from China is removed. See “Wave energy in source region” in the Materials and Methods section for details. **d.** Sum of the size spectral densities plotted in **b** over the basins for observation (black dots) and our model (blue curve). The orange curve and black dashed line denote lognormal distribution and a cube power law, respectively. The observed data and cube power law line are the same as those in Cózar et al’s Fig.S10. The gray dots and curve are the same as the black dots and blue curve, respectively, except that the South Atlantic data is excluded for the sizes less than 30 mm (the digitizer does not recognize the small spectral values above 30 mm for the South Atlantic data in Cózar et al’s figure). The scale of each axis on panels **b** and **d** follows that of Cózar et al’s Figs.S6 and S10, respectively, except that the vertical scale on panel **b** is shown as spectral density. The map in **a** is created using the same softwares as in Figure 3a.

(Fig.3d and S1 Table), which may be due to some local conditions or to the conditions of some remote locations where the microplastics originate. It is indeed possible that some microplastics in this region originate from the Philippine Sea, where wave energy is large [50], as previous studies indicate that some waters from the Philippine Sea are transported into the Seto Inland Sea through the western boundary current [51–53].

Discussion

In summary, we derive a theoretical size distribution of micro- and meso-plastics using a statistical mechanical approach. It assumes that larger “energy” is required to break down the original plastic piece into smaller fragments and that this energy follows the Boltzmann distribution. This model well reproduces observed size distributions from the micro- to meso-plastics. In particular, it naturally explains the rapid decrease toward smaller sizes without invoking a removal of smaller fragments. This model is highly idealized, and extending this model for more realistic fragmentation processes that may be involved is a future study.

As pointed out above, Cózar et al’s South Atlantic size distribution deviates from our theoretical curve more than the other size distributions in the same dataset. S3 Appendix considers theoretical size distributions that would result if the sample is a mixture of plastic pieces originating from various source regions with different values of γ^* , assuming that each source contributes the same number of plastic fragments for simplicity. The resultant superposition deviates from the single-source size distribution in a similar way that Cózar et al’s South Atlantic size distribution deviates from the single-source theoretical distribution (Fig. C in S3 Appendix). Interestingly, the value of $1/\gamma^*$ that best fits the mixture is close to the average of $1/\gamma^*$ values of the origins in this simple example (See “Size distribution” in S3 Appendix).

Similarly, a mixture of plastic fragments produced in various conditions may need to be considered for interpreting the observed total plastic mass. Isobe et al [8] show that the total mass of the plastics for sizes below 5 mm is about 0.3 mg m^{-3} for their samples in the Western-Pacific transoceanic surveys assuming that $\rho = 1000 \text{ kg m}^{-3}$. To obtain this value from our M formula (2) with the optimal values of A and γ^* for their dataset and with $\Lambda = 5 \text{ mm}$, we arrive at a value $\Delta h \approx 1 \text{ mm}$. Obviously this value of Δh is too large for the fragmentation model presented in this study because fragments smaller than Δh cannot be produced by the two-dimensional fragmentation of a plate with a thickness of Δh . This problem may be resolved if the value of Δh obtained like this is in fact an average of the various thicknesses of the original plastic plates (see “Total mass” in S3 Appendix).

Even ignoring the effect of such a mixture, our model implicitly precludes fragments smaller than the lower limit of the thickness of original plastic plates, which is $\sim 100 \mu\text{m}$. In reality, finer microplastics are observed in the ocean and on beaches using different methods from those in Isobe et al.s or Cózar et al [22, 24, 47, 54]. We hypothesize that these finer fragments are produced by secondary fragmentation of microplastics. Since the smaller microplastics are closer to three-dimensional shapes than to a plate, their fracture would be a three-dimensional process.

The 3-dimensional version of our model (Fig. D in S4 Appendix) can be similarly constructed to the 2-dimensional version (Fig. 1a). The result is such that the model spectrum (1) gets one more factor of λ^{-1} and $\gamma^* = \gamma/(3L^3\phi)$, where L' is the size of the original microplastic cube. The peak size is at $\lambda_p = 0.201\gamma^{*-1}$. See S4 Appendix for a complete derivation. The theoretical curves of the 3-dimensional model are found to be in good agreement with the observed size spectra of the fine microplastics with scales of $O(10 \mu\text{m})$ collected near the sea surface [24, 47], in the upper ocean from the surface to the mesopelagic layer [54], and on a beach [22] (Fig. E in S4 Appendix). Those

theoretical curves are characterized by γ^* values of 1.68–14.01 mm⁻¹, which are 10–100 times larger than the two-dimensional γ^* values of 0.24–0.39 mm⁻¹ for Isobe et al.’s [8, 19, 21] and Cózar et al.’s [20] (Figs. 3 and 4). Note that, however, the energy requirement for the fragmentation is given by γ . As an order-of-magnitude calculation, the value of $\gamma = 3L'^3\phi\gamma^*$ from the three-dimensional γ^* value is $O(10^3)$ smaller than the value of $\gamma = 2L^2\Delta h\phi\gamma^*$ from the two-dimensional γ^* value under the reasonable assumptions that $L = 100$ mm and $\Delta h = L' = 1$ mm and that the surface energy density ϕ is the same. This small γ value comes from the smallness of the initial size, L' , which we assume that the three-dimensional fragmentation starts from. Plastics with smaller initial sizes can be fragmented by smaller energy since the surface energy decreases with the initial size (see Figs. 1b in this text and Fig. D in S4 Appendix).

Accordingly, the fate of the marine plastics may be as follows. Original plastic pieces deposited at a beach are fragmented down to millimeter size by weather phenomena such as waves. The two-dimensional version of our model intends to predict the spectrum of these fragments. Those microplastics are further fragmented into finer pieces by slow weathering, grinding in sand, or other processes. The three-dimensional version of our model may also explain the resultant size spectrum of the finer fragments. Both types of microplastics are washed off into the ocean. Given that a smaller particles are susceptible to the vertical mixing [19, 23, 24, 55], those finer microplastics may be spread over the mixed layer or deeper, while the larger ones may tend to stay at the sea surface. This scenario based on our fracture models has no contradiction to the observed evidence on the spatially varying size distribution of the microplastics so far.

It has been hypothesized that the rapid decrease toward the small size in the observed size distribution at the surface indicates the deep intrusion of the finer microplastics. Some numerical simulations incorporating sinking processes qualitatively support this scenario [17, 19, 24], but such a rapid decrease as observed has not been *quantitatively* explained by this process yet. In addition, the trouble is that there have not been observations that measure both large (> 300 μm) and fine (< 300 μm) microplastics at the same time and there is no data showing continuous spectrum over the entire microplastic range. There is not much evidence to prove or disprove this hypothesis.

The main purpose of this paper has been to explain the size distribution of larger microplastics ($> \sim 300$ μm) at the surface, but it has been suggested that the rapid decrease toward the small size common to most size distributions may be an artifact attributable to the method of collection or size detection [24, 25]. However, we note that the observed size distributions in Fig. 3b and d have different peak sizes even though both samples are collected with the neuston nets of the same standards (See “**Observed data in Isobe et al**” of Materials and Methods section, and the original articles [19, 21]). This result suggests that the peak and the small-size drop are real.

In addition, the reduction in the particle count at smallest sizes would be a physically reasonable feature when available fracture energy is limited. Indeed, the general grinding needs larger energy to create smaller particles [56, 57], and the size distribution resulting from a progressive grinding process has this feature [58]. The power law, which the literature often invokes to explain size distributions, is usually ascribed to some progressive fragmentation processes. Such processes may also result in a decrease at small sizes if a limitation of energy is introduced as it is to our model. When the observed spectrum drops at smaller sizes, the lognormal distribution is also often invoked and contrasted to the power law in the literature on experiments for plastic fragmentation [59, 60]. Quantitatively, the lognormal distribution does not much differ from our model spectrum (Figs. 3 and 4) although it does not agree with the power law in the larger-size range (Fig. 4d). Distributions which were compared to the lognormal distribution in the literature may be explained by similar mechanisms to our model.

The present fracture model may open paths toward developing sophisticated numerical simulations for predicting the production and dispersion of the microplastics. There have been numerical simulations to evaluate the spreading microplastics in the ocean [6–9, 61]. In such simulations, virtual parcels representing a mass of plastic pieces are released at source regions and advected by ocean currents. The amount of plastics released has to be either assumed or calibrated so that the resultant mass distribution matches observations. The size distribution, if that information is necessary, is usually assumed in an ad-hoc manner or calibrated against observations. Given that the microplastics are likely to originate from the weathering of plastic litter on beaches [3–5], their size distribution would depend on weather and wave conditions that would be different for each beach. Our size distribution model may be used to estimate the initial size distribution of plastic fragments by parameterizing γ^* at the beaches as a function of weather conditions such as winds and waves.

Materials and methods

Details of fracture model

In the Fracture model section, we only outlined the derivation of our model spectrum and focused on its interpretation; here we show full details of the derivation. Our model is derived in analogy with black body radiation; see [S2 Appendix](#) for the analogy.

In this model, we consider that a square plastic plate with a size of $L \times L$ and a uniform thickness of Δh is broken into $n \times n$ equal-sized cells (Fig. 1a). The size of each broken piece is given by $\lambda = L/n$; we also define an associated “wavenumber” $\nu \equiv \lambda^{-1} = n/L$ for convenience.

In general, the minimal energy required to fracture a lump of solid is given by the surface energy [37], which is proportional to the area of the newly created surface. This area in the present model is proportional to the total length of the contact boundaries (Fig. 1a), which is related to n , like $2L(n-1) \approx 2Ln$. With the aid of $\nu = n/L$, the crush energy for a plate can therefore be written as $b\nu$ with a constant $b \equiv 2L^2\Delta h\phi$, where ϕ is a uniform surface energy density, and hence the crush energy for j plates can be written as

$$\varepsilon \equiv j b \nu. \quad (3)$$

We assume that the occurrence probability of crush energy is governed by the Boltzmann distribution characterized by γ :

$$p(\varepsilon) \propto e^{-\varepsilon/\gamma}, \quad (4)$$

which states that a crush event with a large energy value is less frequent, consistent with common expectation. In statistical mechanics, γ is temperature in heat bath times the Boltzmann constant (Fig. A in [S2 Appendix](#)). This is the analogy to the “environment” for microplastics.

From (3), the expected value of the crush energy as a function of ν is

$$\langle \varepsilon \rangle_{\nu} = \sum_{j=0}^{\infty} j b \nu p(j b \nu) = b \nu \langle j \rangle_{\nu},$$

and from (4),

$$\langle j \rangle_{\nu} = \frac{\sum_{j=0}^{\infty} j e^{-j b \nu / \gamma}}{\sum_{j=0}^{\infty} e^{-j b \nu / \gamma}} = \frac{1}{e^{b \nu / \gamma} - 1}, \quad (5)$$

which is the expected value of the number of fractured plates for each ν . This formula is called the Bose distribution [62]. Since the number of the fragments of a particular size is $n^2 j$ (Fig. 1a) and $n = L\nu$ by definition, the expected number of fragments is $P(\nu) \propto n^2 \langle j \rangle_\nu \propto \nu^2 \langle j \rangle_\nu$ and therefore,

$$P(\nu)d\nu = A\nu^2 \frac{1}{e^{b\nu/\gamma} - 1} d\nu, \quad (6)$$

or converting from ν to λ , we arrive at the size spectrum we already presented in the Fracture model section

$$S(\lambda)d\lambda = \frac{A}{\lambda^4} \frac{1}{e^{b/\lambda\gamma} - 1} d\lambda, \quad (1)$$

where A is an arbitrary positive constant.

Observed data in Isobe et al

The observed size distributions in Isobe et al are from surveys around Japan [21], in a western Pacific transoceanic section [8], and in Seto Inland Sea [19] (Fig. 3a). The first set of samples is from 56 stations around Japan during the period of July 17 through September 2, 2014 [21]. The second is a transoceanic survey at 38 stations across a meridional transect from the Southern Ocean to Japan during 2016 [8]; the stations in Southern Ocean and the other ones were occupied from January 30 to February 4 and from February 12 to March 2, respectively. The third dataset is collected at 15 stations in the Seto Inland Sea of Japan in May–September from 2010 to 2012 [19].

For all surveys, neuston nets with mouth, length, and mesh sizes of $0.75 \times 0.75 \text{ m}^2$, 3 m, 0.35 mm, respectively, were used to sample small plastic fragments. The nets were towed near the sea surface around each station for 20 min at a constant speed of 2–3 knots (1–1.5 m/s). The numbers of fragments are counted for each size bin with a bin width of 0.1 mm for microplastics and 1 mm for mesoplastics (defined to be >5 mm) between 5 and 10 mm, except for the surveys in the Seto Inland Sea, in which the bin width becomes wider beyond the size of 4 mm. The size of a fragment is defined by the longest dimension of its irregular shape. The concentration of the fragments (pieces per unit volume of sea water) within each size bin were calculated by dividing the number of fragments by the water volume measured by the flow meter at each sampling station. This concentration binned according to size is the observational data used in the present study. To obtain the numbers, we have digitized the plots of Isobe et al’s using WebPlotDigitizer version 4.3 (<https://automeris.io/WebPlotDigitizer/>). The original size distributions in the Seto Inland Sea are presented separately for four different areas [19], but they are averaged in the present study.

Figure 5a replots one of these size distributions as an example. As stated above, the bin width is not uniform: for this particular data, $\Delta\lambda = 0.1$ mm for $\lambda < 5$ mm, $\Delta\lambda = 1$ mm for $5 \text{ mm} < \lambda < 10$ mm, and $\Delta\lambda = 10$ mm for $\lambda > 10$ mm. This is the reason that the concentration jumps up beyond $\lambda > 5$ mm. For comparison with theories, we introduce a “size spectral density” n_i (Fig. 5b) such that

$$\Delta\lambda_i n_i = N_i, \quad (7)$$

where $\Delta\lambda_i$ is the width of the i -th bin and N_i is Isobe et al.’s value for the bin. By this definition, each rectangular area of the spectral plot is proportional to the number of plastic fragments within the bin. The spectral density is less sensitive to the bin widths, and in the limit of $\Delta\lambda \rightarrow 0$, it converges to a continuous size spectrum $S(\lambda)$ such that $\int_{\lambda_a}^{\lambda_b} d\lambda S(\lambda)$ is the number of fragments between λ_a and λ_b . All of Isobe et al’s size distributions are converted to size spectral densities in the present study.

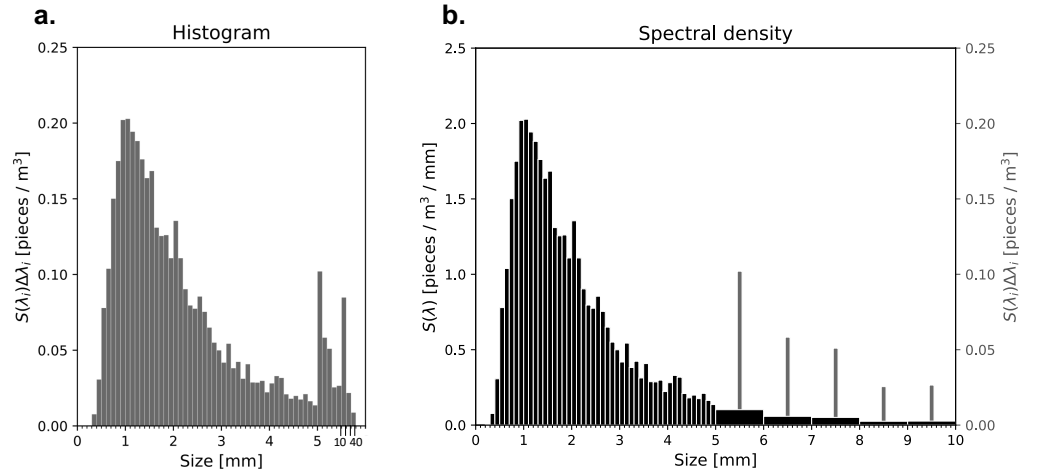


Fig 5. Size distribution expressed as a histogram (a) and as a spectral density (b) from Isobe et al’s [21] observation around Japan. The histogram is a replot of Isobe et al’s Fig2. We have obtained the data by digitizing the original figure using WebPlotDigitizer version 4.3 (<https://automeris.io/WebPlotDigitizer/>). The size spectral density is indicated by black bars with its scale shown on the left axis of panel (b), and the gray bars on panel (b) are the same histogram with its scale on the right axis. The spectral density is plotted in such a way that the black bars exactly coincide with the gray ones for $\lambda < 5$ mm. In panel (b), sizes larger than 10 mm are omitted because the spectral values are almost zero there.

Observed data in C3zar et al

The plastic samples summarized in C3zar et al [20] were collected in the accumulation zones [49] around the world (Fig. 4a) from December 2010 to July 2011. Their method of sampling was the same as that of Isobe et al’s studies, except for the different mesh size (0.2 mm at the minimum) and mouth area ($1 \times 0.5 \text{ m}^2$) of the neuston net and the different towing durations (10–15 min). The collected plastic fragments are classified into bins whose widths increase exponentially (like $\Delta\lambda_k = c10^{0.1k}$ mm, where k is the bin number) for $0.2 \text{ mm} < \lambda < 100 \text{ mm}$.

C3zar et al summed the number of plastic pieces over each accumulation zone without dividing the number by the volume of the sampled sea water (Fig. S6 in their paper). Their data are digitized and converted to spectral densities in the same way as described above for Isobe et al’s data. Sizes larger than 40 mm in the tail of the distribution have had to be omitted because the numbers are so small there that the data points are too close to the horizontal axis of the plots for the digitizer to resolve. This limitation does not significantly influence the curve fitting because the fitting result is most highly sensitive to the values of the size spectral density around the peak size. The present study has also digitized C3zar et al’s Fig. S10b to create a logarithmic plot of the sum of the size distributions for all the observed accumulation zones (Fig. 4d).

Wave energy in source region

We use the Lebreton et al’s plastic dispersal simulation result [48] to identify the source regions of the plastic fragments sampled in the C3zar et al’s accumulation zones. Lebreton et al’s numerical simulation provides the dispersion of virtual particles representing a set of plastic fragments originating from land following the sea-surface currents reproduced by an oceanic circulation modelling system HYCOM/NCODA [63]. The particles are released at coastal locations on the basis of two scenarios, the amount

of released particles determined as a function of impervious surface area (ISA-based scenario) and of coastal population density (PD-based scenario), respectively. The former is intended to reflect contributions from major rivers and the latter from large cities. Contribution in percentage of each emission region to the amount of the plastics in the accumulation zones are summarized in Table 1 from Lebreton et al’s supplementary data. For example, the plastic emission from Australia accounts for about 9.5% of the amount of plastics found in the South Pacific accumulation zone for the ISA scenario.

Next, we estimate wave energy level (no units) at each emission region from the 6-grade wave energy levels along the global coastlines provided by Fairley et al [50]. Each of Lebreton et al’s emission regions for each emission scenario consists of multiple emission points (their supplementary figures S2–S7). We select the point with the largest emission within the region, look up Fairley et al’s figure to determine the wave energy level of the point, and assign the energy level to the region. If there are multiple points with similarly large energy levels, we assign the average energy level to the region. These energy levels are summarized in the “Energy Level” column of Table 1; the left and right subcolumns are for the ISA and PD scenarios, respectively. Some of the energy level values are missing in the table because the selected emission points are not covered in Fairley et al’s map. Finally, the expected wave energy level that the plastics found in the accumulation zone experienced for each scenario is calculated by the contribution-weighted average $\sum_i E_i f_i / \sum_i f_i$, where E_i and f_i denote the wave energy level and the contribution of the i -th source region, respectively. For the North Pacific, we calculate the expected wave energy level without contribution from China, assuming that plastic wastes from China go to the North Pacific accumulation zone via Japan. The resultant expected wave energy level for each accumulation zone is shown in S1 Figure.

Supporting information

S1 Appendix Derivation of total abundance.

S2 Appendix Analogy with black body radiation.

S3 Appendix Superposition of size distributions.

S4 Appendix Three-dimensional model for fine microplastics.

S1 Figure Expected wave energy level (no units) for accumulation zone in Southern Indian Ocean (SIO), North Atlantic (NA), North Pacific (NP), South Atlantic (SA), and South Pacific (SP) (blue bars).

S1 Table Optimal γ^* for different observation regions.

Acknowledgments

This research was benefited from interactions and discussions with Ettore Barbieri, Hiroki Fukagawa, and Yosuke Nakata (alphabetical order). The observed data were obtained by digitizing the published original figures with WebPlotDigitizer version 4.3 (<https://automeris.io/WebPlotDigitizer/>).

Table 1. Expected wave energy levels (based on Fairley et al’s [50] map) at source regions and plastic emissions (percentage) that contribute to the five major oceanic accumulation zones based on the two terrestrial release scenarios (ISA scenario and PD scenario) from Lebreton et al [48]. The categorization of the source regions is from Lebreton et al’s supplementary material. The values for the ISA and PD scenarios are indicated in the left and right sub-columns of each column, respectively. See the Methods section for the details.

Sources	Wave energy level		Accumulation zones									
			SIO		NA		NP		SA		SP	
Aus	5	5	0.089	0.185			0.000	0.000	0.005	0.009	9.502	15.976
NZ	5	5	0.017	0.002			0.000		0.035	0.006	31.211	4.213
South Am wst	3	3	0.007	0.001			0.049	0.084	0.020	0.001	20.376	35.645
South Am est	2	2	7.530	4.435	5.317	6.570			58.530	79.591	1.538	0.986
Cent Am est	2	2			13.294	20.841						
North Am est	1	2			50.281	44.931						
Cent Am wst	4	4	0.006	0.000	0.018		3.793	0.589			5.532	1.457
North Am wst	4	4	0.003	0.003			8.822	7.337			0.056	0.062
Canada wst	5	5	0.000	0.000	0.151		0.569	0.205				
Africa est	2	2	25.872	7.434				0.000	5.982	3.861	9.422	2.873
Africa wst	3	6	2.779	0.676	4.194	5.076			33.906	13.386	0.412	0.148
Africa Nth	3.5	3.5			1.908	5.672				0.001		
Arabia	1	1	0.410	1.001					0.017	0.088	0.050	0.106
Med	1	1										
Asia SE	1	1	10.748	5.509			1.131	0.695	0.155	0.163	4.142	2.218
Indonesia	1	1	27.645	60.278			1.603	5.094	0.381	1.826	13.495	30.801
China	1	2	7.243	11.588			65.784	58.036	0.076	0.227	2.456	4.114
Russia est			0.024	0.007	0.134		7.385	0.742			0.007	0.002
Black Sea												
North Europe	1	6			24.004	16.836		0.000	0.000			
Canada est					0.555							
GreenLnd												
Russia wst					0.144	0.075						
India wst	2	2	5.136	3.311					0.238	0.306	0.537	0.473
India est	2	2	12.294	4.991				0.652	0.652	0.523	1.165	0.655
Japan	5	5	0.197	0.578			10.863	27.217	0.010	0.012	0.099	0.271
Expected wave energy level			1.6	1.4	1.3	3.0	1.8	2.9	2.3	2.5	3.3	2.7
							Without China →		3.2	4.1		
Expected wave energy level (Ave.)			1.5		2.1		2.3		2.4		3.0	
							Without China →		3.7			

References

1. Jambeck JR, Geyer R, Wilcox C, Siegler TR, Perryman M, Andrady A, et al. Plastic waste inputs from land into the ocean. *Science*. 2015;347(6223):768–771.
2. Barnes DK, Galgani F, Thompson RC, Barlaz M. Accumulation and fragmentation of plastic debris in global environments. *Philos Trans R Soc B*. 2009;364(1526):1985–1998.
3. Corcoran PL, Biesinger MC, Grifi M. Plastics and beaches: a degrading relationship. *Mar Pollut Bull*. 2009;58(1):80–84.
4. Andrady AL. Microplastics in the marine environment. *Mar Pollut Bull*. 2011;62(8):1596–1605.
5. Andrady AL. The plastic in microplastics: A review. *Mar Pollut Bull*. 2017;119(1):12–22.
6. Eriksen M, Lebreton LC, Carson HS, Thiel M, Moore CJ, Borerro JC, et al. Plastic pollution in the world's oceans: more than 5 trillion plastic pieces weighing over 250,000 tons afloat at sea. *PLoS ONE*. 2014;9(12):e111913.
7. Van Sebille E, Wilcox C, Lebreton L, Maximenko N, Hardesty BD, Van Franeker JA, et al. A global inventory of small floating plastic debris. *Env Res Lett*. 2015;10(12):124006.
8. Isobe A, Iwasaki S, Uchida K, Tokai T. Abundance of non-conservative microplastics in the upper ocean from 1957 to 2066. *Nat Commun*. 2019;10(1):1–13.
9. Onink V, Wichmann D, Delandmeter P, Van Sebille E. The role of Ekman currents, geostrophy, and Stokes drift in the accumulation of floating microplastic. *J Geophys Res: Oceans*. 2019;124(3):1474–1490.
10. Ashton K, Holmes L, Turner A. Association of metals with plastic production pellets in the marine environment. *Mar Pollut Bull*. 2010;60(11):2050–2055.
11. Holmes LA, Turner A, Thompson RC. Adsorption of trace metals to plastic resin pellets in the marine environment. *Environ Pollut*. 2012;160:42–48.
12. Nakashima E, Isobe A, Kako S, Itai T, Takahashi S. Quantification of toxic metals derived from macroplastic litter on Ookushi Beach, Japan. *Environ Sci Technol*. 2012;46(18):10099–10105.
13. Browne MA, Dissanayake A, Galloway TS, Lowe DM, Thompson RC. Ingested microscopic plastic translocates to the circulatory system of the mussel, *Mytilus edulis* (L.). *Environ Sci Technol*. 2008;42(13):5026–5031.
14. Boerger CM, Lattin GL, Moore SL, Moore CJ. Plastic ingestion by planktivorous fishes in the North Pacific Central Gyre. *Mar Pollut Bull*. 2010;60(12):2275–2278.
15. Murray F, Cowie PR. Plastic contamination in the decapod crustacean *Nephrops norvegicus* (Linnaeus, 1758). *Mar Pollut Bull*. 2011;62(6):1207–1217.
16. Jabeen K, Su L, Li J, Yang D, Tong C, Mu J, et al. Microplastics and mesoplastics in fish from coastal and fresh waters of China. *Env Res Lett*. 2017;221:141–149.

17. Iwasaki S, Isobe A, Kako S, Uchida K, Tokai T. Fate of microplastics and mesoplastics carried by surface currents and wind waves: A numerical model approach in the Sea of Japan. *Mar Pollut Bull.* 2017;121(1-2):85–96.
18. Sagawa N, Kawai K, Hinata H. Abundance and size of microplastics in a coastal sea: Comparison among bottom sediment, beach sediment, and surface water. *Mar Pollut Bull.* 2018;133:532–542.
19. Isobe A, Kubo K, Tamura Y, Nakashima E, Fujii N, et al. Selective transport of microplastics and mesoplastics by drifting in coastal waters. *Mar Pollut Bull.* 2014;89(1-2):324–330.
20. Cózar A, Echevarría F, González-Gordillo JI, Irigoien X, Úbeda B, Hernández-León S, et al. Plastic debris in the open ocean. *Proc Natl Acad Sci USA.* 2014;111(28):10239–10244.
21. Isobe A, Uchida K, Tokai T, Iwasaki S. East Asian seas: a hot spot of pelagic microplastics. *Mar Pollut Bull.* 2015;101(2):618–623.
22. Eo S, Hong SH, Song YK, Lee J, Lee J, Shim WJ. Abundance, composition, and distribution of microplastics larger than 20 μm in sand beaches of South Korea. *Environ Pollut.* 2018;238:894–902.
23. Reisser JW, Slat B, Noble KD, Plessis KD, Epp M, Proietti MC, et al. The vertical distribution of buoyant plastics at sea: an observational study in the North Atlantic Gyre. *Biogeosciences.* 2015;12:1249–1256.
24. Enders K, Lenz R, Stedmon A Colin, Nielsen G Torkel. Abundance, size and polymer composition of marine microplastics $\leq 10 \mu\text{m}$ in the Atlantic Ocean and their modelled vertical distribution. *Mar Pollut Bull.* 2015;100(1):70–81.
25. Kooi M, Koelmans AA. Simplifying microplastic via continuous probability distributions for size, shape, and density. *Env Res Lett.* 2019;6(9):551–557.
26. Dohnanyi JS. Collisional model of asteroids and their debris. *Journal of Geophysical Research.* 1969;74(10):2531–2554.
27. Davis DR, Weidenschilling SJ, Farinella P, Paolicchi P, Binzel RP. Asteroid collisional history: Effects on sizes and spins. In: Binzel R, Gehrels T, Matthews MS, editors. *Asteroids II.* Univ. of Arizona Press, Tucson.; 1989. p. 805–826.
28. Tanaka H, Inaba S, Nakazawa K. Steady-state size distribution for the self-similar collision cascade. *Icarus.* 1996;123(2):450–455.
29. Kolmogorov A. On the logarithmic normal distribution of particle sizes under grinding. In: *Dokl. Akad. Nauk SSSR.* vol. 31; 1941. p. 99–101.
30. Middleton G. Generation of the log-normal frequency distribution in sediments. In: *Topics in mathematical geology.* Springer; 1970. p. 34–42.
31. Crow EL, Shimizu K. *Lognormal Distributions: Theory and Applications.* Marcel Dekker, New York; 1988.
32. Vincent P. Differentiation of modern beach and coastal dune sands—a logistic regression approach using the parameters of the hyperbolic function. *Sedimentary Geology.* 1986;49(3):167 – 176. doi:[https://doi.org/10.1016/0037-0738\(86\)90036-9](https://doi.org/10.1016/0037-0738(86)90036-9).
33. Kobayashi N, Kohyama K, Sasaki Y, Matsushita M. Statistical laws for food fragmentation by human mastication. *J Phys Soc Japan.* 2006;75(8):083001.

34. Ishii T, Matsushita M. Fragmentation of Long Thin Glass Rods. *J Phys Soc Japan*. 1992;61(10):3474–3477. doi:10.1143/jpsj.61.3474.
35. Weibull W. Wide applicability. *Journal of applied mechanics*. 1951;103(730):293–297.
36. Brown WK, Wohletz KH. Derivation of the Weibull distribution based on physical principles and its connection to the Rosin–Rammler and lognormal distributions. *J Appl Phys*. 1995;78(4):2758–2763. doi:10.1063/1.360073.
37. Butt HJ, Graf K, Kappl M. *Physics and chemistry of interfaces*. John Wiley & Sons; 2013.
38. Biswas S, Ray P, Chakrabarti BK. *Statistical physics of fracture, breakdown, and earthquake: effects of disorder and heterogeneity*. John Wiley & Sons; 2015.
39. de Vladar HP, Barton NH. The contribution of statistical physics to evolutionary biology. *Trends Ecol Evol*. 2011;26(8):424 – 432. doi:<https://doi.org/10.1016/j.tree.2011.04.002>.
40. Bouchet F, Venaille A. Statistical mechanics of two-dimensional and geophysical flows. *Phy Rep*. 2012;515(5):227 – 295. doi:<https://doi.org/10.1016/j.physrep.2012.02.001>.
41. Vallianatos F, Papadakis G, Michas G. Generalized statistical mechanics approaches to earthquakes and tectonics. *Proc Math Phys Eng Sci*. 2016;472(2196):20160497. doi:10.1098/rspa.2016.0497.
42. Wu W, McFarquhar GM. Statistical Theory on the Functional Form of Cloud Particle Size Distributions. *J Atmos Sci*. 2018;75(8):2801–2814. doi:10.1175/jas-d-17-0164.1.
43. Kittel C, Kroemer H. *Thermal physics*. 2nd ed. W. H. Freeman and Company; 1980.
44. Holthuijsen LH. *Waves in Oceanic and Coastal Waters*. Cambridge University Press; 2007. Available from: <https://doi.org/10.1017%2F9780511618536>.
45. Tuomi L, Kahma KK, Pettersson H. Wave hindcast statistics in the seasonally ice-covered Baltic Sea. *Boreal Env Res*. 2011;16:451–472.
46. Haselsteiner AF, Thoben KD. Predicting wave heights for marine design by prioritizing extreme events in a global model. *Renew Energ*. 2020;156:1146–1157. doi:<https://doi.org/10.1016/j.renene.2020.04.112>.
47. Poulain M, Mercier MJ, Brach L, Martignac M, Routaboul C, Perez E, et al. Small microplastics as a main contributor to plastic mass balance in the North Atlantic subtropical gyre. *Environ Sci Technol*. 2018;53(3):1157–1164.
48. Lebreton LCM, Greer SD, Borrero JC. Numerical modelling of floating debris in the world’s oceans. *Mar Pollut Bull*. 2012;64(3):653 – 661. doi:<https://doi.org/10.1016/j.marpolbul.2011.10.027>.
49. Maximenko N, Hafner J, Niiler P. Pathways of marine debris derived from trajectories of Lagrangian drifters. *Mar Pollut Bull*. 2012;65(1-3):51–62.

50. Fairley I, Lewis M, Robertson B, Hemer M, Masters I, Horrillo-Caraballo J, et al. A classification system for global wave energy resources based on multivariate clustering. *Appl Energy*. 2020;262:114515. doi:<https://doi.org/10.1016/j.apenergy.2020.114515>.
51. Takeoka H, Akiyama H, Kikuchi T. The Kyucho in the Bungo Channel, Japan—Periodic intrusion of oceanic warm water. *J Oceanogr*. 1993;49(4):369–382.
52. Isobe A, Guo X, Takeoka H. Hindcast and predictability of sporadic Kuroshio-water intrusion (kyucho in the Bungo Channel) into the shelf and coastal waters. *J Geophys Res: Oceans*. 2010;115(C4).
53. Nagai T, Hibiya T. Numerical simulation of tidally induced eddies in the Bungo Channel: A possible role for sporadic Kuroshio-water intrusion (kyucho). *J Oceanogr*. 2012;68(5):797–806.
54. Pabortsava K, Lampitt RS. High concentrations of plastic hidden beneath the surface of the Atlantic Ocean. *Nat Commun*. 2020;11(1). doi:10.1038/s41467-020-17932-9.
55. Kukulka T, Proskurowski G, Morét-Ferguson S, Meyer D, Law K. The effect of wind mixing on the vertical distribution of buoyant plastic debris. *gryl*. 2012;39(7).
56. Berk Z. *Food process engineering and technology*. Academic press; 2018.
57. Duroudier JP. *Size Reduction of Divided Solids*. Elsevier; 2016.
58. Blanc N, Mayer-Laigle C, Frank X, Radjai F, Delenne JY. Evolution of grinding energy and particle size during dry ball-milling of silica sand. *Powder Technol*. 2020;376:661 – 667. doi:<https://doi.org/10.1016/j.powtec.2020.08.048>.
59. Timár G, Blömer J, Kun F, Herrmann HJ. New universality class for the fragmentation of plastic materials. *Phys Rev Lett*. 2010;104(9):095502.
60. Kishimura H, Noguchi D, Preechasupanya W, Matsumoto H. Impact fragmentation of polyurethane and polypropylene cylinder. *Physica A*. 2013;392(22):5574–5580.
61. Wichmann D, Delandmeter P, van Sebille E. Influence of near-surface currents on the global dispersal of marine microplastic. *J Geophys Res: Oceans*. 2019;124(8):6086–6096.
62. Bose SN. Planck’s law and light quantum hypothesis. *Z Phys*. 1924;26(1):178.
63. Cummings JA. Operational multivariate ocean data assimilation. *Quart J Royal Met Soc, Part C*. 2005;131(613):3583–3604.

Supporting Information for
“A model for the size distribution of marine microplastics: a
statistical mechanics approach”
Aoki and Furue

S1 Appendix Derivation of total abundance

In this section, we calculate the total number and total mass of the plastic fragments. In the main text, the amplitude A is nondimensional when $S(\lambda)$ is fitted to an observed size spectrum per unit volume of sea water or it has the dimension of length cubed when the observation is a raw size spectrum as in Cózar et al. Accordingly, the following total number and mass are regarded as per unit volume of sea water or raw depending on which type of size spectrum $S(\lambda)$ denotes.

A transformation of variables $\nu' = \nu/\gamma^*$ in (6) leads to

$$S(\nu)d\nu = A\gamma^{*3}\nu'^2 \frac{1}{e^{\nu'} - 1} d\nu'. \quad (\text{S1})$$

The total number of plastic fragments over $0 < \lambda < \Lambda$ ($\leq L$) can then be written as

$$N \equiv \int_{1/\Lambda}^{\infty} S(\nu)d\nu = \int_{1/\gamma^*\Lambda}^{\infty} \frac{A\gamma^{*3}\nu'^2}{e^{\nu'} - 1} d\nu' \quad (\text{S2})$$

and with this familiar formula $(e^{\nu'} - 1)^{-1} = \sum_{j=1}^{\infty} e^{-j\nu'}$,

$$\begin{aligned} N &= A\gamma^{*3} \sum_{j=1}^{\infty} \int_{1/\gamma^*\Lambda}^{\infty} \nu'^2 e^{-j\nu'} d\nu' \\ &= A\gamma^{*3} \left[2\text{Li}_3(e^{-1/\gamma^*\Lambda}) + 2 \left(\frac{1}{\gamma^*\Lambda} \right) \text{Li}_2(e^{-1/\gamma^*\Lambda}) - \left(\frac{1}{\gamma^*\Lambda} \right)^2 \ln(1 - e^{-1/\gamma^*\Lambda}) \right], \end{aligned} \quad (\text{S3a})$$

where

$$\text{Li}_s(z) \equiv \sum_{j=1}^{\infty} \frac{z^j}{j^s}.$$

When $\Lambda \gg \gamma^{*-1}$,

$$N \approx A\gamma^{*3} 2\text{Li}_3(1) = \sigma A\gamma^{*3}, \quad (\text{S3b})$$

where $\sigma \equiv 2.404$, because $\text{Li}_3(1) = \sum_{j=1}^{\infty} j^{-3} \simeq 1.202$ (known as Apéry's constant; see <https://oeis.org/A002117>). This approximation is equivalent to $\int_{1/L}^{\infty} S(\lambda)d\lambda \approx \int_0^{\infty} S(\lambda)d\lambda$. This approximation is a natural one when $\Lambda \sim L$ because $1/\gamma^*\Lambda \sim 1/\gamma^*L = 2L\Delta h\phi/\gamma$ and this factor is therefore the ratio of the surface energy $L\Delta h\phi$ to the mean environmental energy γ . We naturally assume that $L\Delta h\phi \ll \gamma$ because otherwise not many small fragments would be generated.

Similarly, the total mass of plastics is

$$M \equiv \int_0^{\Lambda} \rho\lambda^2 \Delta h S(\lambda)d\lambda, \quad (\text{S4})$$

where ρ is the mass density of the plastic material and Δh is the thickness of the original plate. After similar transformations as above,

$$M = A\gamma^* \rho \Delta h \sum_{j=1}^{\infty} \frac{e^{-j/\gamma^*\Lambda}}{j} = -A\gamma^* \rho \Delta h \ln(1 - e^{-1/\gamma^*\Lambda}) \quad (\text{S5a})$$

$$\approx A\gamma^* \rho \Delta h \ln(\gamma^*\Lambda), \quad (\text{S5b})$$

using the same approximation, $\gamma^*\Lambda \gg 1$, as for N . Unlike N , M depends on Λ even when $\gamma^*\Lambda \gg 1$ because the contribution of larger plastic pieces is significant to M whereas it is negligible to N .

S2 Appendix Analogy with black body radiation

Our size spectrum is derived in analogy with black body radiation. Here we outline the derivation of the wavenumber spectrum of black body radiation and discuss the analogy. Since the derivations of the Boltzmann distribution and Planck's spectrum below are standard, we do not cite references there. See the literature on statistical mechanics for details (e.g., Kittel and Kuroemer 1980 [43]).

Boltzmann distribution. Consider a large isolated system (heat bath) and a small subsystem, and classify the states which the subsystem can take by their energy value E . Assume that the subsystem takes a state with E at a probability of $p(E)$. Then we calculate the probability distribution that maximizes the entropy of the subsystem,

$$S = -k \int_0^{\infty} [p(E) \ln p(E)] \Omega(E) dE, \quad (\text{S6})$$

where $\Omega(E)$, known as the “density of states,” is the number of states with energy value E in the subsystem, under the constraints that $\int_0^{\infty} p(E) dE = 1$ and that the expected value of energy

$$\langle E \rangle = \int_0^{\infty} E p(E) \Omega(E) dE \quad (\text{S7})$$

is given. The solution is

$$p(E) = \frac{e^{-\beta E}}{Z}, \quad \text{where } Z \equiv \int_0^{\infty} e^{-\beta E} \Omega(E) dE. \quad (\text{S8})$$

The variable Z as a function of β is called the “partition function”.

This probability distribution is known as the Boltzmann distribution. The variable β , which enters the solution because of the energy constraint, is related to the temperature of the system through the thermodynamic relation

$$\frac{1}{T} = \frac{\partial S}{\partial \langle E \rangle} = \beta k.$$

For the second equality, we have used (S6)–(S8) to calculate the derivative. We replace β with kT in what follows.

Black body radiation. Consider a mass of material, a “black body”, which is in thermal equilibrium and assume that there is a vacuum cavity within it. Photons are emitted from the black body into the vacuum cavity and absorbed by the opposite wall. The energy of the photons obeys the energy probability distribution of the black body, which is assumed to be the Boltzmann distribution. Planck further assumed that the energy of a photon with frequency ω can take only a value which is an integral multiple of the unit $\hbar\omega$, where \hbar is a universal constant. The energy of the photons in the cavity, accordingly, takes the form of

$$\varepsilon(j, \omega) = j\hbar\omega. \quad (\text{S9})$$

Since (S9) obeys the Boltzmann distribution, we can convert the probability of photon energy as a function of j with ω regarded as a parameter using (S9) and (S8). The result is $p(j; \omega) = e^{-j\hbar\omega/kT} / \sum_j e^{-j\hbar\omega/kT}$. In this case, the expected energy can be calculated as $\langle E \rangle = \sum_j j\hbar\omega p(j; \omega)$ and hence

$$\langle E \rangle(\omega) = \frac{\hbar\omega}{e^{\hbar\omega/kT} - 1} \quad (\text{S10})$$

for each frequency. Also, this energy divided by $\hbar\omega$ provides the expected number of photons

$$\frac{1}{e^{\hbar\omega/kT} - 1}. \quad (\text{S11})$$

This formula is known as the Bose distribution.

Finally, we convert the energy distribution (S10) to the frequency spectrum of energy considering the dimensionality of the space. The frequency interval $(\omega, \omega + d\omega)$ includes ω^2/π^2c^3 modes of the wave per unit volume of the three-dimensional cavity. Since the energy spectrum is the product between the number of modes included in the interval $(\omega, \omega + d\omega)$ and the expected value of the energy at ω , which is given by (S10), the result is Planck's energy spectrum

$$\frac{\hbar}{\pi^2c^3} \frac{\omega^3}{e^{\hbar\omega/kT} - 1}. \quad (\text{S12})$$

Analogy. By analogy, the photons correspond to the fragmented plastic litters on beaches, and the black body to the environment (the weather and wave conditions) (Fig. A). The mean energy of the black body, kT , corresponds to the mean crush energy, γ , of the environment. Further, the crush energy is expressed as $\varepsilon = j b \nu$ (Eq. 3) on the basis of the necessary surface energy. This expression corresponds to (S9) in Planck's theory. Because of this analogy, the Boltzmann distribution (Eq. 4 with Eq. 3) and the Bose distribution (Eq. 5) in our model are formally the same as those of Planck's theory.

Our size spectrum (Eqs. 1 and 6) is analogous to Planck's (S12). As compared to (6), Planck's formula can be obtained formally if we take $A \rightarrow \hbar/\pi^2c^3$ and $\gamma \rightarrow kT$, $\nu \rightarrow \omega$ after multiplying the right-hand side of (6) by ν . The last multiplication is merely due to the dimensionality of the space: the numerator of our formula becomes also proportional to ν^3 if the fragmentation of plastics is three-dimensional (see below). The corresponding wavelength (size) spectrum is obtained from the relation $\lambda = c/2\pi\omega$ for Planck's and $\lambda = 1/\nu$ for our spectrum.

The transition from (S10) to (S12) does not have a close analogy with the plastic model. As we have seen, Planck's energy distribution is essentially

$$(\text{number of modes} \propto \omega^2) \times (\text{energy of a photon } \hbar\omega) \times (\text{Bose distribution})$$

On the other hand, our plastic "wavenumber" spectrum is essentially

$$(\text{number of fragments} \propto \nu^2) \times (\text{Bose distribution}),$$

where the Bose distribution describes the expected number of original plastic pieces (plates) which are fragmented. If the original plastic piece is a cube and its fragmentation is three-dimensional, the number of fragments will be proportional to ν^3 and the functional form of the plastic "wavenumber" distribution with respect to ν will be exactly the same as Planck's (See S4 Appendix).

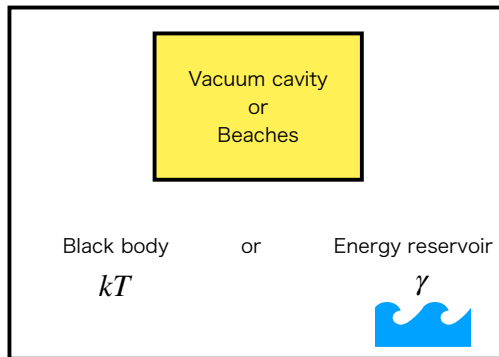


Fig. A. Analogy between black-body radiation and microplastics. The yellow area represents the vacuum cavity where electromagnetic radiation occurs or the beaches where microplastics are produced. The white area represents the blackbody characterized by kT , or the energy reservoir (winds, waves, and so on) characterized by γ .

S3 Appendix Superposition of size distributions

Size distribution. We explore how the size distribution is modified if multiple source regions with different parameters contribute. Here we assume that each source region contributes the same number of plastic fragments (N), which gives A in (1) as a function of γ^* :

$$A = \frac{N}{\sigma\gamma^{*3}} = \frac{N}{2.404\gamma^{*3}}$$

according to (2). In this case, the size spectrum (1) can be written as

$$S^*(\lambda; a, b^*) \equiv a \frac{b^{*3}}{\lambda^4} \frac{1}{e^{b^*/\lambda} - 1},$$

where a is a nondimensional constant and $b^* \equiv b/\gamma = 1/\gamma^*$.

We next calculate the average of $S^*(\lambda; 1, b^*)$ from $b_c^* - \Delta b^*/2$ to $b_c^* + \Delta b^*/2$. The order of magnitude of b^* is known because the value of λ that gives the peak of the size spectrum is $O(b^*)$ (it can be shown that it is approximately $0.255b^*$ from Eq. 1 and this λ value is constrained by observations). The average is calculated numerically changing b^* at an interval of 0.1 mm. For an illustration, and we look at three cases with $(b_c^*, \Delta b^*) = (4 \text{ mm}, 4 \text{ mm}), (7 \text{ mm}, 4 \text{ mm}), (5 \text{ mm}, 8 \text{ mm})$, and plot the results in Figs. Ba, Bc, and Be, respectively. The solid black curve plots the averaged S^* ; the dashed and dotted curves plot $S^*(\lambda; 1, b_1^*)$ and $S^*(\lambda; 1, b_2^*)$, where $b_1^* \equiv b_c^* - \Delta b^*/2$ and $b_2^* \equiv b_c^* + \Delta b^*/2$.

We then fit $S^*(\lambda; a, b^*)$ to the average profile by adjusting a and b^* , which is the red curve. This is to simulate the fitting of our theoretical curve to an observation which may be a mixture of plastic pieces from different origins. Compared to the “pure” profile (red curve), the peak of the average profile (black curve) shifts leftward, the peak value is lower, and the values are larger in the smallest size range.

The right panels of Fig. B plot the error (cyan curve) of the fitting of the pure profile to the average as a function of Δb^* with the same b_c^* value as in the respective left panel, which corresponds to the maximum value of Δb^* of the right panel. As expected, the fitting error grows with Δb^* . The green curve plots the optimal b^* as a function of Δb^* . The optimal b^* changes little and stays close to b_c^* (thin gray line), indicating that the value of b^* ($= 1/\gamma^*$ by definition) obtained by fitting observations is close to its average value.

Fig. C plots the average and optimal profiles from Fig. Ba but with the horizontal axis logarithmic (panel a) and with both axes logarithmic (panel b). The difference between the two curves is qualitatively similar to the difference between the observed and the best-fit theoretical curves for Cózar et al’s South Atlantic data in Fig. 4d.

Total mass. Here we explore the impacts of superposition on the total mass. Suppose that the observed size distribution is a superposition of different distributions with different values of A , γ , ϕ , L , and Δh (See Fig. 1). We denote those parameter values for each distribution by A_k , γ_k , etc. for $k = 1, \dots, K$. Assume that the shape of the superposition is similar to a “pure” distribution as in Figs. Ba and Bc.

By fitting our model spectrum to the observed, we obtain optimal values for b^* and A . Because the size distribution is similar to the corresponding “pure” distribution, (S5a) or (S5b) should give an accurate total mass. In the main text, we used this approach to infer the value of Δh so that the calculated total mass agrees with the observed. This approach can be formulated by, if we use the approximate form (S5b) for simplicity,

$$\frac{\rho\Delta h A}{b^*} \ln(\Lambda/b^*) = \sum_{k=1}^K \frac{\rho_k A_k}{c_k} \ln \frac{\Lambda}{c_k \Delta h_k},$$

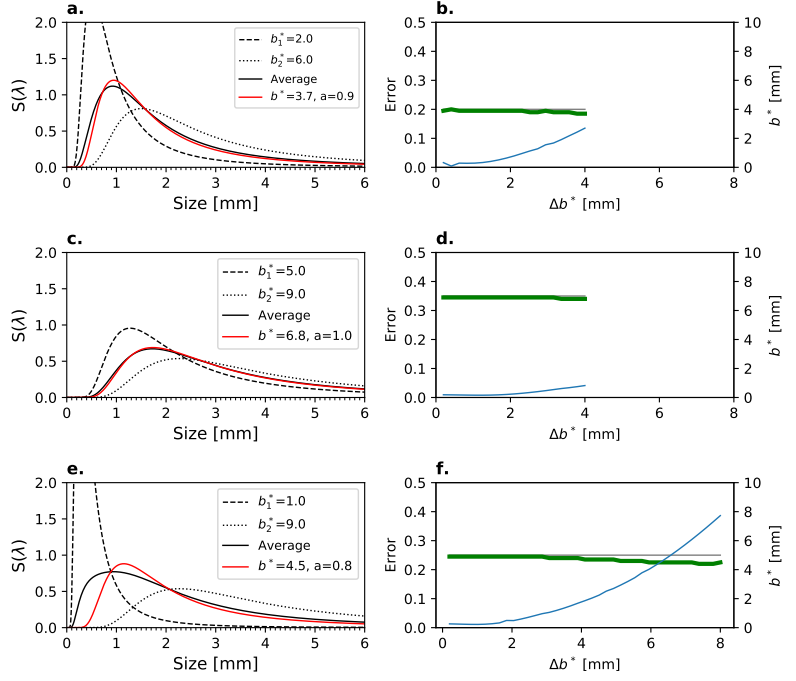


Fig. B. Superposition of size distributions with different values of b^* ($= 1/\gamma^*$) ranging from $b_c^* - \Delta b^*/2$ to $b_c^* + \Delta b^*/2$ for (a) $b_c^* = 4$ mm and $\Delta b^* = 4$ mm, (c) $b_c^* = 7$ mm and $\Delta b^* = 4$ mm, and (e) $b_c^* = 5$ mm and $\Delta b^* = 8$ mm. The dashed and dotted curves on the left panels are $S(\lambda; 1, b_1^*)$ and $S(\lambda; 1, b_2^*)$, respectively, where $b_{1,2}^* \equiv b_c^* \pm \Delta b^*/2$. The solid black curve is $S(\lambda; 1, b^*)$ averaged from b_1^* to b_2^* . The red curve indicates the best-fit size spectral density $S(\lambda; a_{\text{opt}}, b_{\text{opt}}^*)$ to the average. The right panels (b,d,f) show the fitting error (cyan) and the optimal b^* of the best-fit curve (green) as a function of Δb^* , where b_c^* and the maximum value of Δb^* are the same as in the corresponding left panel. The error is defined as the ratio of the norm of the difference between the average and best-fit curves to the norm of the average. The thin horizontal gray line denotes b_c^* .

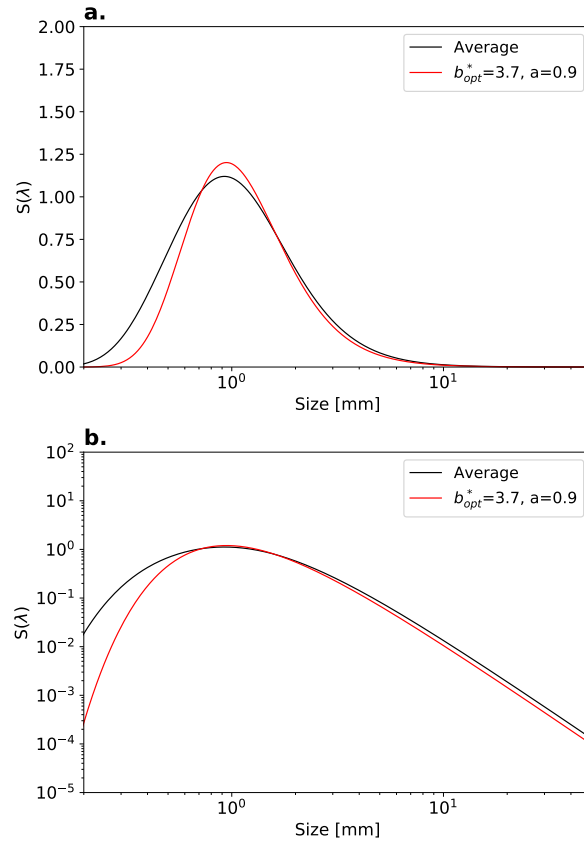


Fig. C. Size spectral density averaged over b^* (black) and the best-fit curve (red) with optimal values for b^* and a . Both curves are the same as the black and red curves of Fig. Ba except the horizontal axis (a) and both axes (b) are logarithmic in this figure.

where $c_k \equiv b_k^*/\Delta h_k = 2L_k^2\phi_k/\gamma_k$. The values of A and b^* on the left-hand side are those obtained by fitting the observed distribution and Δh on the left-hand side is the inferred value. Therefore, the inferred Δh is an “average” of Δh_k ’s in the sense that

$$\Delta h = \frac{b^*}{\rho A \ln(b^*/\Lambda)} \sum_{k=1}^K \frac{\rho_k A_k}{c_k} \ln \frac{c_k \Delta h_k}{\Lambda}.$$

Obviously, the result depends on the parameters A_k , γ_k , etc. If, for example, we assume that the each source contributes an equal number of plastic fragments (N), then $A_k = b_k^{*3} N/\sigma = (c_k \Delta h_k)^3 N/\sigma$, and the resultant dependency of the inferred Δh on Δh_k is

$$\Delta h = \frac{b^*}{\rho A \ln(b^*/\Lambda)} \sum_{k=1}^K \frac{\rho_k c_k^2 \Delta h_k^3 N}{\sigma} \ln \frac{c_k \Delta h_k}{\Lambda}.$$

S4 Appendix Three-dimensional model for fine microplastics

Our plate model presented in the Fracture model section and the Materials and Methods section (Fig. 1) implicitly allows for fragmented cells whose lateral size λ is smaller than the thickness Δh of the original plate. It is not very realistic to produce such small fragments from two dimensional fragmentation only and we do not attempt to apply our two-dimensional fracture model directly to plastic fragments for which $\lambda \ll \Delta h$. We instead construct a three-dimensional version of our model to explain fine microplastics ($\sim 10 \mu\text{m} < \lambda < \sim 300 \mu\text{m}$) recently observed in the upper ocean or on a beach [22, 24, 47, 54]

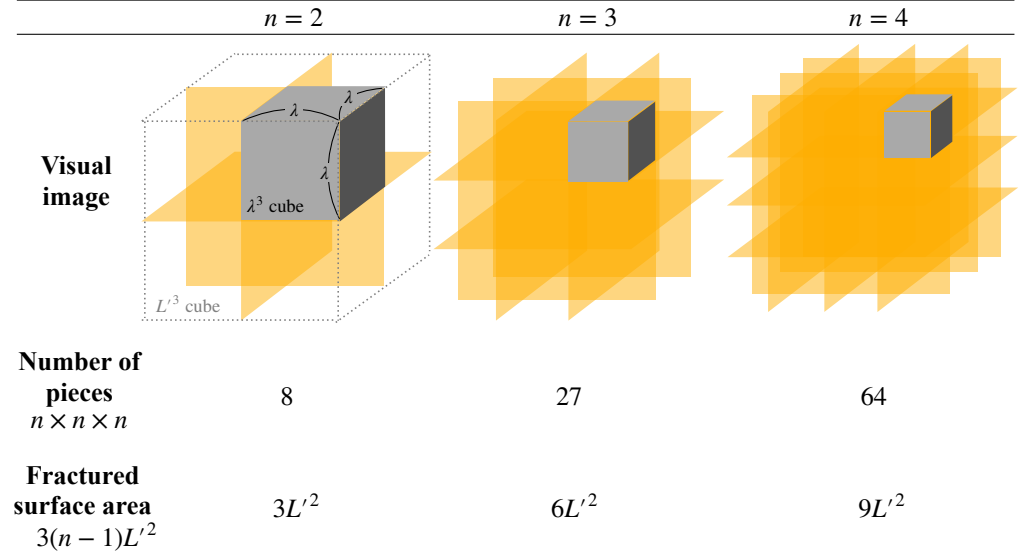


Fig. D. Schematic representation of 3-dimensional fracture model. All idealized plastic cube with a volume of L'^3 is broken into $n \times n \times n$ (middle) small cubes with the equal size of $\lambda = L'/n$. Orange planes show the surface created by the breakage and the total area of the planes depending on n is shown at the bottom.

Three-dimensional model. As an extension of the plate model, we consider the fracture of a cube with a volume of L'^3 into $n \times n \times n$ equal-sized cubic cells. Schematics are shown in Figure D. The cell size is then $\lambda = L'/n$; with use of its inverse $\nu \equiv n/L'$, similarly to the original plate model, the number of pieces of the cells can be expressed as $L'^3 \nu^3$. Also, the area of the new surfaces produced in this breakage is $3(n - 1)L'^2$, which is proportional to n and hence to ν when $n \gg 1$. This allows defining the crush energy as $\varepsilon = j b \nu$, where j is the number of L'^3 cubes to be fractured and $b \equiv 3L'^3 \phi$. Since this crush energy is formally the same as for the original plate model (3), the expected number of the fragments is given by the same Bose distribution as (5). Thus, the size spectrum for the 3-dimensional model can be expressed as

$$P(\nu)d\nu = A\nu^3 \frac{1}{e^{\nu/\gamma^*} - 1} d\nu \quad \text{or} \quad (\text{S13})$$

$$S(\lambda)d\lambda = \frac{A}{\lambda^5} \frac{1}{e^{1/\lambda\gamma^*} - 1} d\lambda, \quad (\text{S14})$$

where we have defined $\gamma^* \equiv \gamma/b$ as in the main manuscript. These formulae are the same as (6) and (1) except for the exponents on ν and λ , respectively. For a large size

limit, i.e., $\lambda\gamma^* \gg 1$, Eq. S14 asymptotes to $A\gamma^*/\lambda^4$. Also, the peak size is approximately $\lambda_p \simeq 0.201/\gamma^*$. In the similar fashion to the original plate model (See S1 Appendix), the total mass of the fragments in the size range from 0 to Λ ($\Lambda \leq L'$) is calculated as

$$M \equiv \int_0^\Lambda \rho\lambda^3 S(\lambda) d\lambda$$

$$= -\rho A\gamma^* \ln(1 - e^{-1/\gamma^*\Lambda}) \quad (\text{S15})$$

$$\simeq \rho A\gamma^* \ln(\gamma^*\Lambda). \quad (\text{S16})$$

Observed data. The 3-dimensional fracture model is applied to four observed size distributions of fine microplastics smaller than 300 μm . First, we compare with the size distribution obtained in the North Atlantic Ocean by Pabortsava and Lampitt [54] (PL2020). This data is the largest collection ($N = 1444$) of microplastics with sizes of $32 \mu\text{m} < \lambda < 651 \mu\text{m}$ in the wide depth range from 10 m to 200 m. Since this collection, however, does not include any data near the sea surface, we also compare with the observed size distributions in the North Atlantic Ocean obtained by Enders et al [24] (EN2015) and Poulain et al [47] (PO2019) to complement this lack. The former collected finer microplastics with $11 \mu\text{m} < \lambda < 300 \mu\text{m}$ sizes at ~ 3 m depth ($N = 543$), and the latter those with $25 \mu\text{m} < \lambda < 500 \mu\text{m}$ sizes in the water very close to the sea surface within 6 cm ($N = 520$). Further, we compare with the observed size distribution ($20 \mu\text{m} < \lambda < 1000 \mu\text{m}$) obtained on Korean beach by Eo et al [22] ($N = 273738$), which could be considered as representative of the microplastics near the origin of their production. The size of the plastic pieces for all these observations is identified by the longest dimension. Additionally, EN2015 and PO2019 also use the geometric mean $\sqrt{d_L d_W}$, where d_L and d_W denote the length and width.

Application. The observed size distributions generally indicate an increase toward small size and sudden drop after passing the peak size for all data except for that in EN2015 (Fig. E). This feature is qualitatively similar to that of the microplastics collected using the neuston net with the mesh size of 300 μm (cf. Figs. 3 and 4). Using the optimal A and γ^* obtained by the least square method over the entire size range, the theoretical curves of the 3-dimensional fracture model are found to well match the observed size distributions. The optimal theoretical curve also reproduces the increase toward small size even for the size distribution in EN2015, which does not have a sudden drop. In this size range, the 3-dimensional fracture model seems to have higher reproducibility for PL2020 and EO2018 than the 2-dimensional model while the difference between the models is not clear for the other cases.

Note that we have chosen geometric mean for size in Figs. Ec and Eb. When plotted with longest dimension, they are respectively Figs. Fa and Fb. Our model fits better with geometric mean (Figs. Ec and Eb) in both cases. For EN2015, our model underestimates in the size range larger than 0.05 mm (Fig. Fa) and this tendency is weakened with geometric mean (Fig. Ec). That is, geometric mean shifts larger fragments leftward in this case. This is a natural consequence of geometric mean. For PO2019, geometric mean not only shifts the data leftward but also smooths the distribution. The distribution is still not quite smooth, suggesting that more samples would be needed to get a smooth distribution. Even with geometric mean, our model still underestimates for sizes larger than 0.05 mm for EN2015 (Figs. Ec and Fa). This might be because some of the samples were collected using a 50 μm (0.05 mm) mesh in some locations [24].

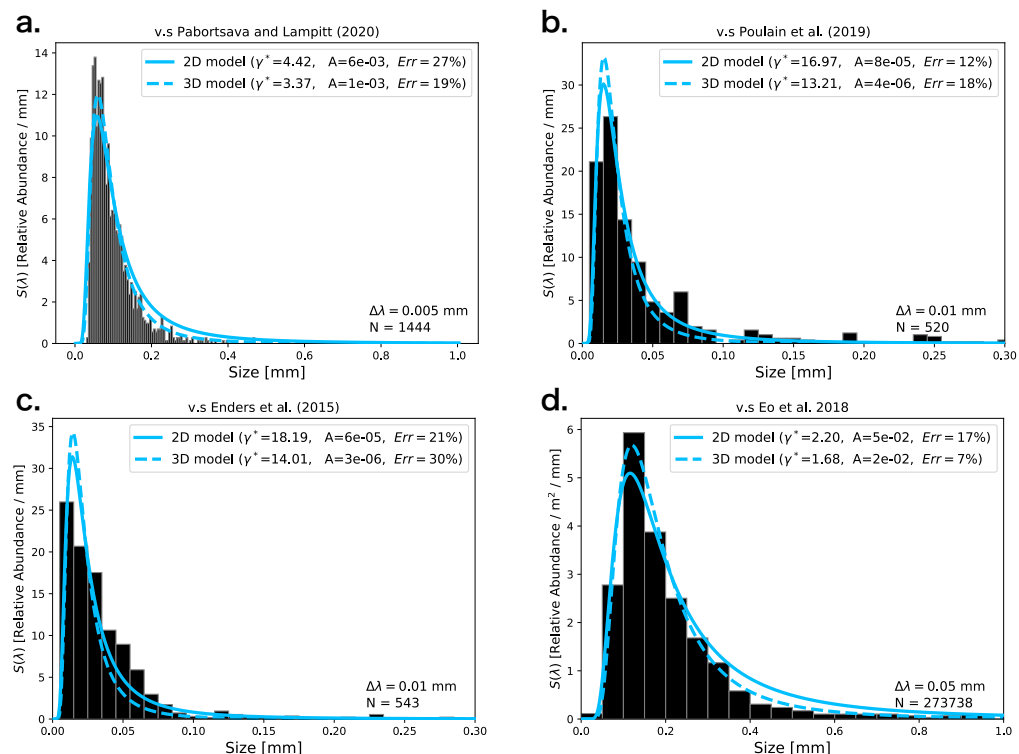


Fig. E. Size spectral densities of fine microplastics for observations (Black bars) and theories based on the original 2-dimensional plate model (Solid blue) and 3-dimensional model (Dashed blue). See Methods for conversion from histogram into size spectrum for the observed data. The observed data are obtained by digitizing the published original figures with WebPlotDigitizer (see the Materials and Methods section), except that the size distribution in **a** is constructed from the fragment size data. Pabortsava and Lampitt [54] plot their data separately for a few depth ranges and polymer types. We have downloaded their data and merged all the data without any weights to construct the spectrum. The spectrum is normalized by the total abundance N . The sizes of the collected fragments for **b** and **c** are defined as geometric mean (see “Observed data” in this Appendix).

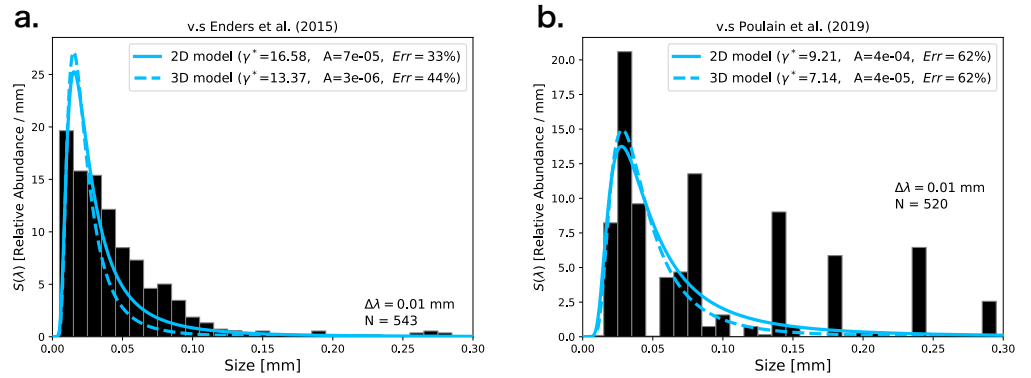
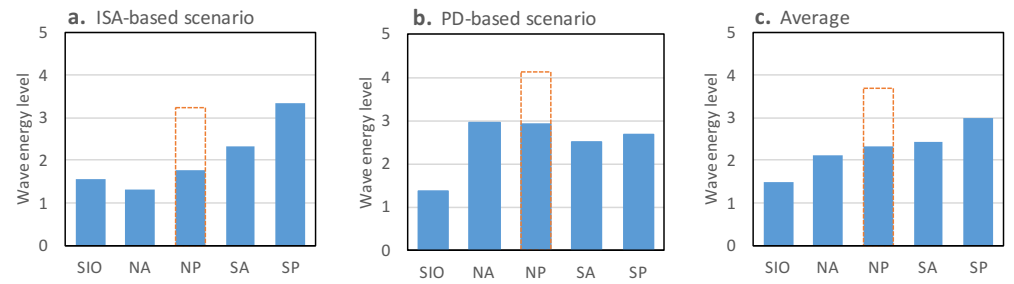


Fig. F. Panels **a** and **b** are respectively the same as Figs. **Ec** and **Eb** except that the size of collected fragments is defined as the longest dimension in these plots.

S1 Figure



S1 Figure. Expected wave energy level (no units) for accumulation zone in Southern Indian Ocean (SIO), North Atlantic (NA), North Pacific (NP), South Atlantic (SA), and South Pacific (SP) (blue bars). Dashed orange bars denote the case without the contribution from China in the North Pacific accumulation zone.

S1 Table

S1 Table. Optimal γ^* for different observation regions

Environmental energy γ^* [mm⁻¹]	Region	Literature
0.24	North Atlantic Ocean	Cózar et al. 2014
0.24	Around Japan	Isobe et al. 2015
0.26	Western Pacific transoceanic section	Isobe et al. 2019
0.27	South Indian Ocean	Cózar et al. 2014
0.27	South Atlantic Ocean	Cózar et al. 2014
0.35	North Pacific Ocean	Cózar et al. 2014
0.35	South Pacific Ocean	Cózar et al. 2014
0.39	Seto Inland Sea	Isobe et al. 2014